Pergamon

Int. J. Heat Mass Transfer. Vol. 37, No. 6, pp. 977–987, 1994

0017–9310/94 $6.00 + 0.00

0017–9310(93)E0006–3

Effect of dynamic perturbation and contact condition on edge-defined fiber growth characteristics

WEI SHYY,† SHIN-JYE LIANG† and DANIEL Y. WEI‡

†Department of Aerospace Engineering, Mechanics & Engineering Science, University of Florida, Gainesville, FL 32611, U.S.A. ‡GE Aircraft Engines, Lynn, MA 01910, U.S.A.

(*Received* 17 *February* 1993 *and in final form* 4 *October* 1993)

Abstract—Sapphire fibers for use in both optical sensors and structure composites have been manufactured using the edge-defined film-fed growth (EFG) process. A thermocapillary model based on a combined Lagrangian/Eulerian method has been developed to simulate the dynamic characteristics of the EFG process, subject to the pull speed perturbations. The meniscus behavior is governed by the Young–Laplace equation subject to a specified contact condition at the trijunction point. Two models have been investigated at the trijunction point, including a conventionally adopted static model which fixes the contact angle, and a dynamic model which regulates the contact angle according to the speed and direction of the instantaneous movement of the trijunction point. It has been predicted, and observed experimentally, that the fiber diameter responds to the pull speed perturbation at the corresponding frequency, but the sensitivity of the response decays as the frequency increases. While both the static and dynamic models at trijunction points cause the crystal to vary in size in response to the external fluctuations, their effects are noticeably different, indicating that the conventional models are not adequate to yield accurate predictions in the solidification characteristics dynamically.

1. INTRODUCTION

SAPPHIRE fiber for use in both optical sensors and structure composites has been developed using the edge-defined film-fed growth (EFG) process [1–5], wherein a crystallographically oriented sapphire fiber is grown from a meniscus of molten alumina. The EFG process can yield continuous lengths of sapphire fiber with diameters in the range of 0.05 to 0.25 mm. The fiber grower, schematically shown in Fig. 1, contains three separate main components: the hot zone, the puller system, and the fiber spooling system. The hot zone consists of an inductively heated refractory metal crucible, with the edge-defining dies all enclosed within a water-cooled, environmentally-regulated chamber. The melt is supplied to each die tip from a capillary fed manifold. The puller system consists of a belt puller and a fiber guide. The belt puller utilizes a double belt traction mechanism driven by a precision stepper motor and is monitored with an optical encoder. After the fiber exits the puller, it passes through several pulleys and is wound on spools under regulated tension. Within the hot zone, the fiber growth process begins with seeding at the die tip, which establishes a crystallographic orientation. The puller speed is generally kept constant and the meniscus dimensions and fiber diameter are manipulated through changes in the induction coil power level setting to adjust die tip temperature.

In practice, both the die tip temperature and the puller speed may experience either intentional or unintentional variations in time. The unintentional variations can result from the perturbations to the operating conditions caused by environmental fluctuations, coil power fluctuations, or motor speed irregularities. The intentional variations can be designed to compensate the aforementioned perturbations to achieve a controlled growth process and uniform crystal properties and dimensions.

In the present work, numerical simulations are conducted to analyze the crystal growth characteristics subject to the perturbations in pull speed under conditions typical to the EFG process. Previously, work has been conducted for this problem [6], where the Stefan number,

$$St = \frac{C_{p_l}\Delta T}{\Delta h_f} \tag{1}$$

where C_{p_l} is the specific heat of melt at constant pressure, ΔT is the characteristic temperature, taken as the difference between temperatures at melting point and die tip, and Δh_f is the latent heat of fusion. The value of St is taken as 1, indicating a substantial temperature variation, of the order of several hundred K, from the die tip to the crystal/melt interface. Here, we choose a Stefan number of 0.024, which is more representative of the current state-of-the-art in actual production. Together with ref. [6], the dynamic characteristics of the EFG process under different conditions can be assessed and compared. Furthermore, so far in the literature, the static contact con-

NOMENCLATURE

A	amplitude of external forcing
Bo	Bond number
Bi	Biot number
C_p	specific heat at constant pressure [J g^{-1} K^{-1}]
f	meniscus shape distribution as function of z and t [cm]
g	gravitational acceleration [cm s^{-2}]
G_s	heat flux along the top of the solid phase [W cm^{-2}]
h	(1) height of the melt/solid interface $h(r, t)$[cm] (2) convective heat transfer coefficient [W cm^{-2} K^{-1}]
h_c	height of the trijunction point [cm]
H_c	non-dimensional h_c
Δh_f	latent heat of fusion [J g^{-1}]
k	thermal conductivity [W cm^{-1} K^{-1}]
l	dimensional vertical length of the physical domain [cm]
L	non-dimensional l
p	pressure [dyne cm^{-2}]
r	radius [cm]
r_b	radius of die [cm]
r_c	radius of the trijunction point [cm]
R	non-dimensional radius
St	Stefan number
t	time [s]
T	temperature [K]
T_a	ambient temperature [K]
T_b	base temperature [K]
T_m	melting temperature [K]
u_p	dimensional pull speed [cm s^{-1}]
U_p	non-dimensional pull speed
z	axial coordinate [cm]
Z	non-dimensional vertical coordinate.

Greek symbols

α	thermal diffusivity [cm^2 s^{-1}]
β	thermal expansion coefficient [K^{-1}]
γ	surface tension [dyne cm^{-1}]
Γ	non-dimensional thermal diffusivity
ε	emissivity
θ	non-dimensional temperature
μ	dynamic viscosity [g s^{-1} cm^{-1}]
ν	kinematic viscosity [cm^2 s^{-1}]
ρ	density [g cm^{-3}]
σ	Stefan–Boltzmann constant [5.670×10^{-12} W cm^{-2} K^{-4}]
τ	characteristic time scale [s]
ϕ_A	advancing contact angle [rad]
ϕ_C	instantaneous contact angle of the meniscus at the trijunction point [rad]
ϕ_R	receding contact angle [rad]
ϕ_0	equilibrium contact angle [rad]
Ω	period of external forcing.

Subscripts

a	ambient quantity
g	gas phase
l	liquid phase
r	radius component
s	solid phase
z	vertical component.

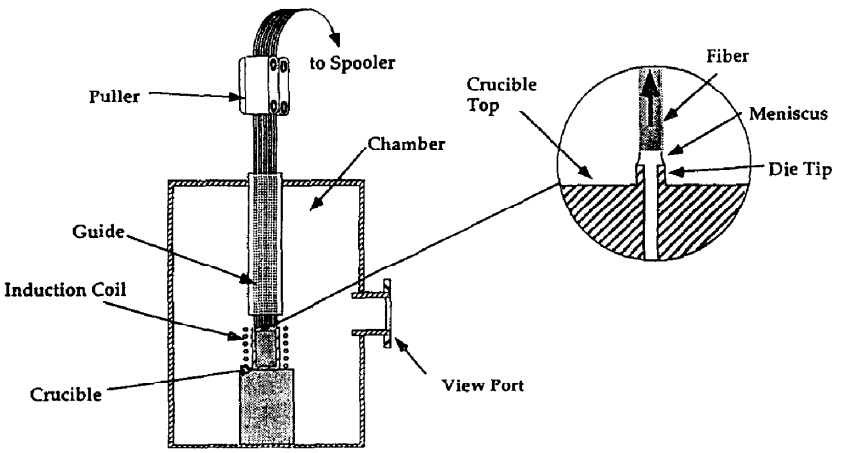

FIG. 1. Schematic illustration of the EFG sapphire fiber growth equipment used to produce 25 fibers with diameters in the range 0.025–0.15 mm. The insert shows a magnified view of the die tip and meniscus region where fiber solidification occurs.

dition is normally adopted [6–8]. In this work, the contact condition at the solid/melt/gas trijunction point is qualitatively extended, and two different types of constraints are compared. They are: (1) the conventional static model which requires that the Young's equilibrium contact condition, namely, a fixed contact angle between the surfaces separating melt/gas and solid/melt be maintained, and (2) a dynamic model which, instead of fixing the contact angle, allows it to vary according to the magnitude and direction of the instantaneous movement of the trijunction point.

The primary focus of the present work is to investigate the effect of perturbation in pull speed, subject to two different models for contact condition at the trijunction point, on the variation of the fiber dimensions. Discussions will also be given regarding the implication of the scaling procedure on computational efficiency. As will be demonstrated, an appropriate scaling procedure should account for the effect of Stefan number of the system, for it regulates the speed of the solid/melt interface movement. Although the focus is on the EFG process, the methodology under development here is generic. It can be applied to study other processing techniques such as Czochralski or floating zone methods.

2. PROBLEM FORMULATION AND NUMERICAL PROCEDURE

A schematic of the present EFG model along with the associated boundary conditions is given in Fig. 2.

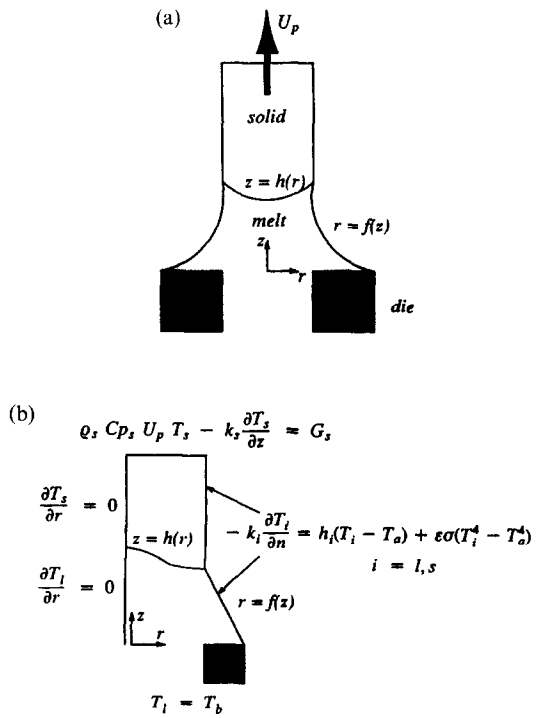

FIG. 2. Schematic of configuration (a) and boundary conditions (b) of the present EFG model.

The physical dimensions and the material properties of sapphire adopted are given in ref. [6]. Table 1 summarizes the important parameters and their numerical values employed in the present model based on these values. Marangoni number can be viewed as the ratio between the time scales associated with heat conduction and shear stress. For a low Prandtl number fluid, where the kinematic viscosity is small com-

Table 1(a). Thermophysical properties and physical dimensions of sapphire (Al_2O_3) and processing parameters used in the present EFG simulation

The material property of sapphire (Al_2O_3)		Adopted value
k_l (W cm^{-1} K^{-1})	0.1	0.1
ρ_l (g cm^3)	3.05	3.05
C_{p_l} (J g^{-1} K^{-1})	1.26	1.26
ε_l	0.9	0.9
k_s (W cm^{-1} K^{-1})	0.1	0.1
ρ_s (g cm^{-3})	4.00	3.05
C_{p_s} (J g^{-1} K^{-1})	1.26	1.26
ε_s		0.9
T_m (K)	2316	2316
Δh_f (J g^{-1})	1046	1046
ϕ_0 (deg)†		135
h (W cm^{-2} K^{-1})		1.1×10^{-3}
r_b (cm)		0.02
ΔT (K)		20
u_p (cm s^{-1})		0.062
β (K^{-1})		3×10^{-5}
γ (dyne cm^{-1})		0.69
σ (W cm^{-2} K^{-4})		5.67×10^{-12}
μ (g cm^{-1} s^{-1})		0.59
ν (cm^2 s^{-1})		0.19

† ϕ_0 is defined as the angle between solid/melt interface and melt/gas interface.

Table 1(b). Definition and magnitude of key dimensionless parameters based on values given in Table 1(a)

$$Fo = \frac{\alpha_l t}{r_b^2}\text{; Fourier number}$$

$$St = \frac{C_p \Delta T}{l_f} = 0.024\text{; Stefan number}$$

$$Bo = \frac{\Delta \rho g r_b^2}{\gamma_{lg}} = 2.8 \times 10^{-4}\text{; Bond number}$$

$$Ra = \frac{\beta g \Delta T r_b^3}{\nu \mu} = 4.2 \times 10^{-5}\text{; Rayleigh number}$$

$$Ma = \frac{\left|\frac{\partial \gamma_{lg}}{\partial T}\right| \Delta T r_b}{\mu \alpha} = 1.56\text{; Marangoni number}$$

$$Pe = \frac{u_p r_b}{\alpha_l} = 0.05\text{; Peclet number}$$

$$Bi = \frac{h r_b}{k} = 2.2 \times 10^{-3}\text{; Biot number}$$

$$Rad = \frac{\varepsilon \sigma r_b \Delta T^3}{k} = 1.8 \times 10^{-9}\text{; Radiation number}$$

pared to the thermal diffusivity, a Marangoni number of order one implies that the velocity scale, other than the constant fiber pull speed, is very small and hence the convection effect resulting from nonuniform surface tension is negligible. The small order of magnitude of the Rayleigh number indicates that the buoyancy-induced convection is also negligible. On the other hand, with a small value of Peclet number, based on the pull speed u_p, the convection effect can be largely neglected. In the present model, the momentum equations are not considered explicitly, but the convective heat transfer caused by the fiber pull speed is accounted for in the energy equation. Some of the basic concepts related to the above issues can be found in Shyy [9]. Capillarity dominates static pressure in terms of controlling the shape of the meniscus. Furthermore, under the condition that hydrostatic pressure is not present, the meniscus profile is close to a straight line [6]. Regarding the governing equations and boundary conditions relevant to the present system, the following presents the Young–Laplace equation (controlling the shape of the melt/gas interface), energy transport equation, mass continuity equation, and movement of the solid/melt interface in the r–z axisymmetric coordinate system.

The Young–Laplace equation governing the equilibrium meniscus shape in the axisymmetric geometry is

$$\gamma_{lg}\left(\frac{f_{zz}}{(1+f_z^2)^{3/2}}-\frac{1}{f(1+f_z^2)^{1/2}}\right)=\Delta\rho g z-\Delta p \quad (2)$$

where γ_{lg} is the surface tension between the melt and the air, f describes the meniscus shape, and Δp is the difference in applied pressure between the liquid phase and the gas phase. The bottom edge of the meniscus is defined by the die radius, r_b, and the top edge is defined by the crystal radius, r_c.

The energy equation in the liquid phase in dimensional form is

$$\rho_l C_{p_l}\left(\frac{\partial T_l}{\partial t}+v_z\frac{\partial T_l}{\partial z}\right)=\frac{1}{r}\frac{\partial}{\partial r}\left(k_l r\frac{\partial T_l}{\partial r}\right)+\frac{\partial}{\partial z}\left(k_l\frac{\partial T_l}{\partial z}\right),$$
$$0\leqslant r\leqslant f(z),\ 0\leqslant z\leqslant h(r) \quad (3)$$

where the subscript l denotes the liquidus phase condition, v_z is the convection speed along the axial direction and f and h define the meniscus shape in the r and z direction, respectively. The boundary conditions are given as follows:

(a) central line

$$\frac{\partial T_l}{\partial r}=0,\quad r=0,\ 0\leqslant z\leqslant h(0) \quad (4)$$

(b) the melt inlet

$$T_l=T_b,\quad 0\leqslant r\leqslant r_b,\ z=0 \quad (5)$$

where T_b is the base temperature at the melt inlet, and r_b is the radius of the contact line between the meniscus and die, and

(c) along the side surface of the melt, heat is transferred to the surroundings by the combined conduction, convection and radiation

$$-k_l\frac{\partial T_l}{\partial n}=h_l(T_l-T_a)+\varepsilon\sigma(T_l^4-T_a^4),$$
$$r=f(z),\ 0\leqslant z\leqslant h_c \quad (6)$$

where n is normal unit vector on the meniscus surface, h_l the heat transfer coefficient, ε the emissivity, σ the Stefan–Boltzmann constant, T_a the ambient temperature, and h_c the height of trijunction point.

Similarly, the energy equation in the solid phase is

$$\rho_s C_{p_s}\left(\frac{\partial T_s}{\partial t}+u_p\frac{\partial T_s}{\partial z}\right)=\frac{1}{r}\frac{\partial}{\partial r}\left(k_s r\frac{\partial\theta_s}{\partial r}\right)+\frac{\partial}{\Delta z}\left(k_s\frac{\partial T_s}{\partial z}\right),$$
$$0\leqslant r\leqslant r_c,\ h\leqslant z\leqslant l \quad (7)$$

where the subscript s denotes the solidus phase condition, r_c is the radius of the trijunction point, and l is the height of the domain modelled. As to the boundary conditions,

(a) along the side surface of the solid, heat is transferred to the surroundings by the combined conduction, convection and radiation

$$-k_l\frac{\partial T_s}{\partial n}=h_s(T_s-T_a)+\varepsilon\sigma(T_s^4-T_a^4),$$
$$r=r(z),\quad h(r_c)\leqslant z\leqslant l \quad (8)$$

(b) along the top boundary of the solid, the heat flux is specified

$$\rho_s C_{p_s}u_p T_s-k_s\frac{\partial T_s}{\partial z}=G_s,\quad 0\leqslant r\leqslant r(l),\ z=l \quad (9)$$

where G_s is the prescribed heat flux out of the top boundary from the crystal, and

(c) along the centerline a symmetric condition is applied

$$\frac{\partial T_s}{\partial r}=0,\quad r=0,\ h(0)\leqslant z\leqslant l. \quad (10)$$

Because of the low Peclet number, convection does not affect heat transfer in a significant way. The velocity in the melt is determined using the one-dimensional continuity equation:

$$(\pi r_0^2)U_p=(\pi r^2)v_z \quad (11)$$

where v_z is the advection speed in the melt, which is determined by the local radius.

Finally, at the melt/solid interface $z=h(r,t)$, both equilibrium solidification and conservation of energy are satisfied.

$$T_l=T_s=T_m \quad (12)$$

$$k_l\frac{\partial T_l}{\partial n}-k_s\frac{\partial T_s}{\partial n}=\rho_l\Delta h_f\left(u_p-\frac{\partial h}{\partial t}\right)_n. \quad (13)$$

Since the equations possess the various dimensionless parameters far from order 1, an appropriate

scaling has been found to be critical in obtaining the solutions in an efficient manner. This aspect will be addressed later.

The computational strategy designed here utilizes an explicit front tracking technique, based on a combined Lagrangian and Eulerian approach, to locate and advance the moving boundaries between the crystal and the melt, as well as the new meniscus shape. The procedure has been discussed in detail in ref. [10]. In this procedure, the markers along the interface are used to define and advance the location of the interface in time; the movement is tracked via a Lagrangian framework. The velocity of each marker is determined by the balance between the difference of thermal gradients in the solid and in the melt, and the latent heat absorption as given in equation (13). Based on the newly defined boundary shapes, a grid will be generated again and the rate of grid movement evaluated accordingly. The energy equation in each phase will be computed in an Eulerian framework. All these procedures are performed in a fully coupled manner involving interactions among the temperature field, meniscus and interface motion, and grid movement at each iteration. Within each time step, the iterations continue until all the governing equations, boundary conditions, and interface constraints are satisfied within a specified convergence criterion; here, it is required that the summation over the domain of the absolute imbalance of the non-dimensional fluxes in each computational cell be smaller 5×10^{-5}.

The various issues of the specification of an appropriate contact condition at the trijunction point have been discussed by Shyy *et al.* [11]. Conventionally, a constant contact angle, in the spirit of the Young's equilibrium contact condition, has been used [10], namely,

$$\frac{dr_c}{dt} = \left(u_p - \frac{dh_c}{dt}\right) \tan(\phi(t) - \phi_0) \qquad (14)$$

where r_c is the radius of the trijunction point, h_c is the height of the trijunction point, $\phi(t)$ is the instantaneous contact angle of the meniscus at the trijunction point measured with respect to a reference direction, ϕ_0 is the equilibrium contact angle which is a material property.

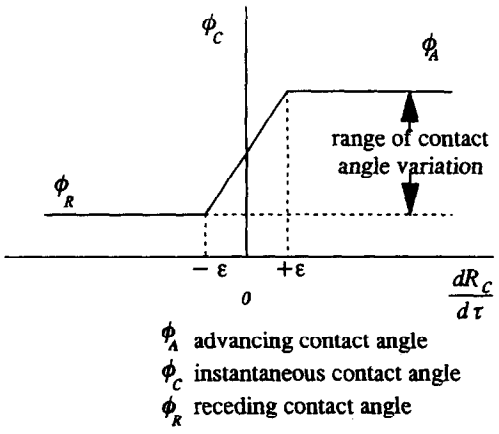

FIG. 3. Model of dynamic contact condition at the trijunction point.

A dynamic condition has also been developed and incorporated into the computational model. This model is depicted in Fig. 3, which indicates that depending on the direction and speed of movement of the trijunction point, the contact angle will assume different values. Specifically, as the rate of change of the radius of a trijunction point exceeds a threshold, namely, $dr_c/dt > \varepsilon$, where ε is a specified value, a constant advancing contact angle is assigned; based on this contact angle, equation (14) is invoked to determine r_c. Similarly, if $dr_c/dt < -\varepsilon$, a different constant receding contact angle is assigned to determine r_c. For dr_c/dt lying between $-\varepsilon$ and ε, the contact angle varies with dr_c/dt, which will determine the instantaneous shape and location of the melt/crystal interface. In this dynamic model, which specified advancing and receding contact angles [7, 11], a qualitative investigation of the effect of contact angle on the solidification characteristics can be made.

Both the static and dynamic contact conditions have been considered in the simulations and their relative impact on the solidification process is assessed. It appears that the conventionally utilized static model [6, 8] at the trijunction point is not sufficient to describe the dynamics of fiber growth. In the following, results obtained from the simulations of the crystal growth process with respect to the pull speed perturbation and different contact conditions are discussed.

3. RESULTS AND DISCUSSION

3.1. *Scaling procedure*

First we discuss two scaling procedures utilized to nondimensionalize and, more critically, normalize the various terms present in the governing equations and their implications on the computational efficiency. As it turns out, due care should be taken in choosing the appropriate reference quantities because for many phase change problems this choice has a major impact on the amount of computing cost in conducting a simulation. It is noted that in the present problem, the two energy transport equations are applied in the regions separated by a moving interface, causing a nonlinear coupling between the two equations. Hence, in the course of solving these energy equations with the backward Euler time stepping scheme, while a von Neumann type of stability analysis indicates that the computation is unconditionally stable for each of the energy equations, the nonlinear coupling caused by the interface movement makes it only conditionally stable. Numerical experiments indicate that, as expected, the range of the time step size acceptable for a stable computation depends on the distribution of the grid points in each phase.

Table 2. Two different scaling procedures and resulting nondimensional energy equations

(a) Choice 1

length scale: $l_r = r_b$, velocity scale: $v_r = \alpha_l/l_r$, time scale: $t_r = l_r/v_r$, and temperature scale: ΔT = difference between temperature at melting point and at die tip.

$$\text{energy equation for melt}: \quad \frac{\partial\theta_l}{\partial\tau} + V_z\frac{\partial\theta_l}{\partial Z} = \frac{1}{R}\frac{\partial}{\partial R}\left(R\frac{\partial\theta_l}{\partial R}\right) + \frac{\partial}{\partial Z}\left(\frac{\partial\theta_l}{\partial Z}\right)$$

$$\text{energy equation for solid}: \quad \frac{\partial\theta_s}{\partial\tau} + U_p\frac{\partial\theta_s}{\partial Z} = \alpha\left[\frac{1}{R}\frac{\partial}{\partial R}\left(R\frac{\partial\theta_s}{\partial R}\right) + \frac{\partial}{\partial Z}\left(\frac{\partial\theta_s}{\partial Z}\right)\right]$$

$$\text{interface movement equation}: \quad \frac{\partial\theta_l}{\partial N} - k\frac{\partial\theta_s}{\partial N} = \frac{\rho}{St}\left(U_p - \frac{\partial H}{\partial\tau}\right)_N$$

where $R = r/l_r$, $Z = z/l_r$, $U_p = u_p/v_r$, $V_z = v_z/v_r$, $\tau = t/t_r$, $\theta_l = (T_l - T_m)/\Delta T$, $\theta_s = (T_s - T_m)/\Delta T$, $\rho = \rho_s/\rho_l$, and $\alpha = \alpha_s/\alpha_l$.

(b) Choice 2

length scale: $l_r = r_b$, velocity scale: $v_r = St\,\alpha_l/l_r$, time scale: $t_r = l_r/v_r$, and temperature scale: ΔT

$$\text{energy equation for melt}: \quad St\left(\frac{\partial\theta_l}{\partial\tau} + V_z\frac{\partial\theta_l}{\partial Z}\right) = \frac{1}{R}\frac{\partial}{\partial R}\left(R\frac{\partial\theta_l}{\partial R}\right) + \frac{\partial}{\partial Z}\left(\frac{\partial\theta_l}{\partial Z}\right)$$

$$\text{energy equation for solid}: \quad St\left(\frac{\partial\theta_s}{\partial\tau} + U_p\frac{\partial\theta_s}{\partial Z}\right) = \alpha\left[\frac{1}{R}\frac{\partial}{\partial R}\left(R\frac{\partial\theta_s}{\partial R}\right) + \frac{\partial}{\partial Z}\left(\frac{\partial\theta_s}{\partial Z}\right)\right]$$

$$\text{interface movement equation}: \quad \frac{\partial\theta_l}{\partial N} - k\frac{\partial\theta_s}{\partial N} = \rho\left(U_p - \frac{\partial H}{\partial\tau}\right)_N$$

Due to the symmetry of the problem, only half of the physical domain is modelled. For the entire physical domain encompassing both the crystal and the melt, effectively a 41×41 nonuniform grid is employed. More details can be found in ref. [6].

Table 2 presents two different scaling procedures and the resulting nondimensional equations of energy transport and interface movement. As can be seen, the only difference between the two procedures is the velocity scale; in choice 1, a standard characteristic diffusional velocity is used, while in choice 2, the Stefan number is included in addition to the diffusional velocity scale. The main motivation of the second choice stems from the observation that as can be easily deduced from equation (13), with choice 1, the nondimensional speed of interface movement is scaled with St. Accordingly, in nondimensional terms, for the low St cases, the interface moves at a correspondingly slow rate. As already mentioned, even with the use of an implicit procedure, the computation is not unconditionally stable. Numerical experiments have indicated that, in terms of the nondimensional values, the time step sizes of the set of governing equations resulting from both choice 1 and 2 have very comparable stability restrictions. Hence, considering the fact that the time scale of choice 2 is larger than that of choice 1 by a factor of $1/St$, the relative computing efficiency of the two scaling procedures depends highly on the value of the Stefan number. As an illustration, computations have been conducted using both scaling procedures and starting with the identical initial conditions for the low St case studied here. In both computations, the nondimensional time step is $\Delta\tau = 10^{-3}$, which is about 10 times the nondimensional diffusional time scale based on the smallest grid spacing, namely $(\Delta x)^2_{\min}/\alpha$, where $(\Delta x)_{\min}$ is the smallest grid spacing and α is the thermal diffusivity. For both scaling procedures, numerical experiments indicate that this value of $\Delta\tau$ is very close to the stability limit of the implicit Euler time stepping scheme adopted in the present work.

Figure 4 compares the paths of the computing histories with both scaling procedures from an identical initial condition toward the steady-state solution subject to the same boundary conditions given in Section 2. The Stefan number chosen in the present work is 0.024. Substantially different convergent behaviors have been observed between the two scaling procedures. As already mentioned, the differences of the convergence characteristic is largely caused by the different orders of magnitude of the nondimensional interface velocity yielded by the two scaling procedures. With choice 1, the interface speed is of the order of St, while with choice 2, it is of the order of 1. Consequently, choice 2 needs a far fewer number of nondimensional time steps to reach the steady-state solution. With choice 1, however, the system appears to go through a long transient period before it can reach the steady state. As a check, the converged steady-state solution obtained from choice 2 is substituted into the computation based on choice 1, and this solution is immediately accepted as the converged solution, confirming that with both scaling procedures, the computations eventually lead to the same steady-state solution. Although the two scaling procedures result in the same solution, as they should,

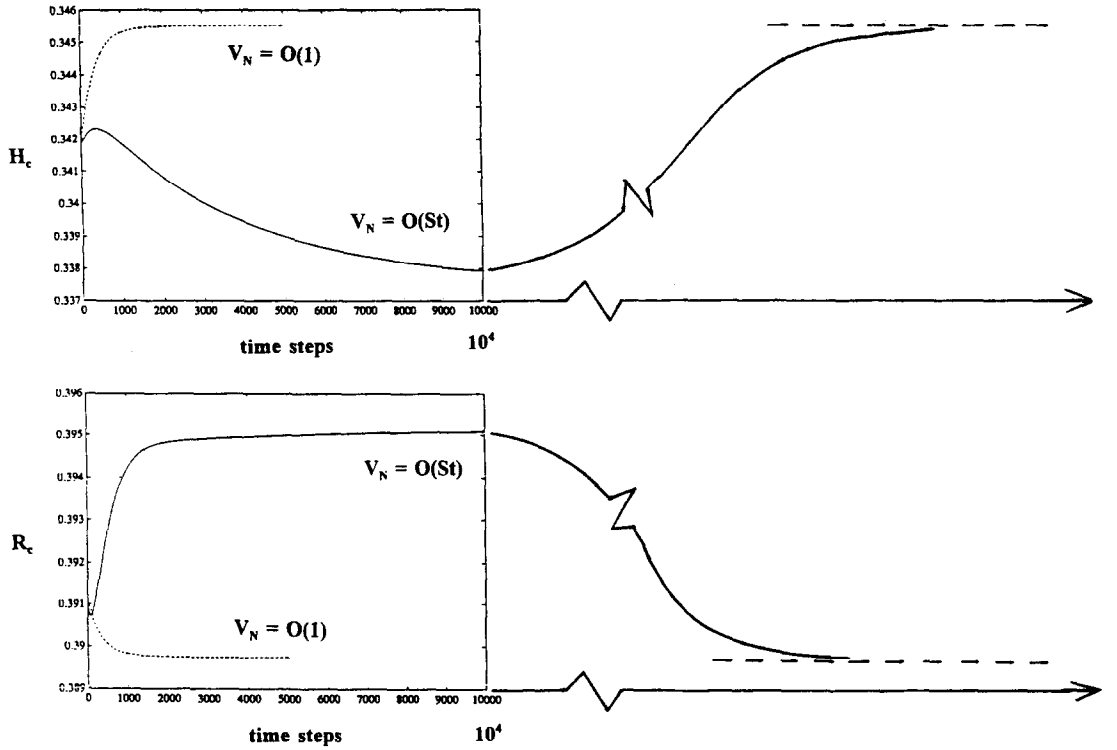

FIG. 4. Comparison of the convergence path of H_c and R_c to reach steady-state using different scaling procedures, choice 1 : $V_N = O(St)$ and choice 2 : $V_N = O(1)$.

the computing cost of them differs by an order of $(1/St)$. For all the results to be presented, the non-dimensional equations based on choice 2 are used. The steady-state isotherm distribution subjected to the conditions given in Table 1 is shown in Fig. 5; due to the small value of Stefan number, the thermal gradients in the melt and the crystal regions are of different magnitudes, as evidenced by the interface constraint listed in Table 2. Furthermore, it is interesting to note that with $St = 0.024$ the solid/melt interface is convex toward the melt, while previously in ref. [6], it is found that with $St = 1$ the interface is convex toward the solid region.

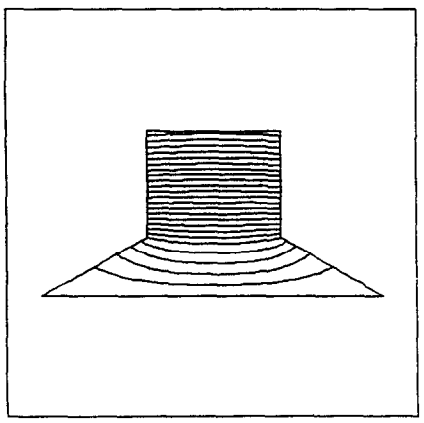

FIG. 5. Isotherms of the steady-state solution corresponding to the operating parameters given in Table 1.

3.2. *Simulation with constant contact angle*

In the course of dynamically simulating the growth characteristics subject to the pull speed perturbations, different frequencies have been investigated. For the results to be presented here, all the boundary conditions remain unchanged except that the pull speed is now composed of the steady-state value plus a fluctuating component which is a sinusoidal function with a fixed frequency, namely,

$$U_p(\tau) = (U_p)_{\text{steady}}[1 + A \sin(2\pi\tau/\Omega)],$$

where $(U_p)_{\text{steady}}$ is the steady state pull speed, A is the percentage of fluctuation and Ω is the period. The simulation starts with the steady-state solution as the initial condition. Figure 6 shows the time series plots of two cases, one with a fluctuating pull speed of the period of $500\Delta\tau$, $\Delta\tau = 10^{-3}$, and another with $20\Delta\tau$. Shown there are the time histories of the pull speed, U_p, the height and the radius of the trijunction point, H_c and R_c, respectively. Consistent with the case of $St = 1$ studied previously [6], the crystal diameter responds to the externally imposed perturbation at the corresponding frequency, but the sensitivity of the response depends on the frequency of perturbation. For a slower perturbation of the period of $500\Delta\tau$, both H_c and R_c exhibit higher levels of oscillation than for a faster perturbation of $20\Delta\tau$; the differences

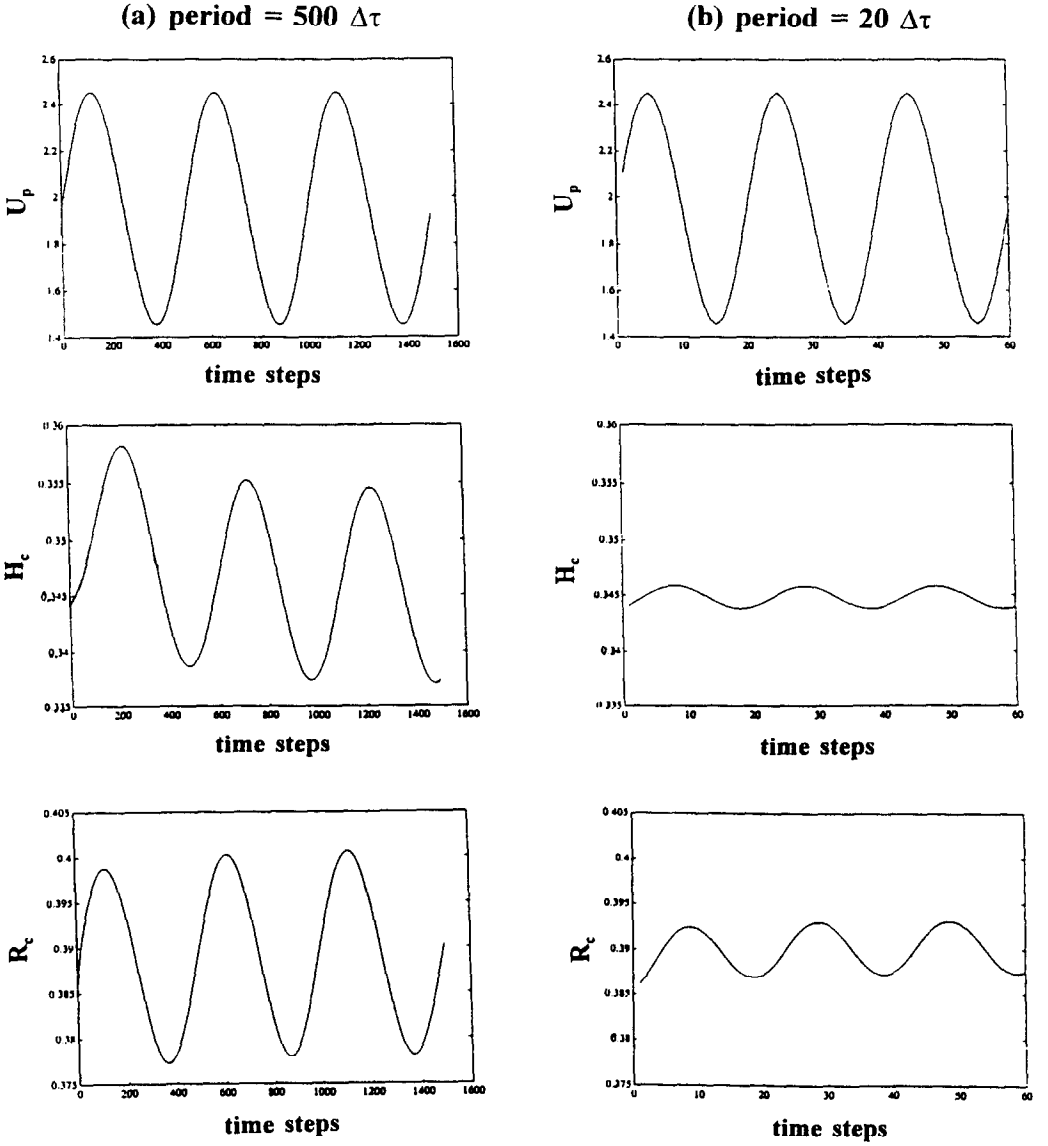

FIG. 6. Time histories of H_c and R_c subject to a single harmonic perturbation of U_p with (a) period = $500\Delta\tau$ and (b) period = $20\Delta\tau$.

between them are substantial. Furthermore, also consistent with the case of $St = 1$, the nonlinearity of the underlying physics has caused the time averaged values of H_c and R_c to be different from the steady-state values.

Figure 7 gives an overall depiction of the percentage variations of H_c and R_c with respect to different perturbation periods predicted by the present model. For both H_c and R_c the tendency of exhibiting reduced sensitivities to the external perturbations as the frequency increases can be clearly observed. The reason for this phenomenon obviously lies in the relative competition of the time scale of the grower and the time scale of the perturbation. Since $\Delta\tau$ is 10^{-3}, for the pull speed fluctuation of the period of several hundred $\Delta\tau$, the system's dominant nondimensional time scale, which is of order 1 according to choice 2 given in Table 2, and the perturbation time scale are comparable. Hence, the system is able to respond and follow the perturbation closely, resulting in a clear connection between the dynamic behaviors of U_p and H_c and R_c. For high frequency perturbations, of the period of hundred $\Delta\tau$ or less, the system's time scale is too long, causing decreases in sensitivity of H_c and R_c as observed in Fig. 7. This phenomenon has also been observed in the actual growth system. Figure 8 shows a Bode diagram based on a series of experiments to depict the frequency response between the fiber diameter and pull speed. It indicates that with relatively slow varying perturbations over a range of frequencies in pull speed, the fiber diameter responds with a certain sensitivity; as the perturbation fre-

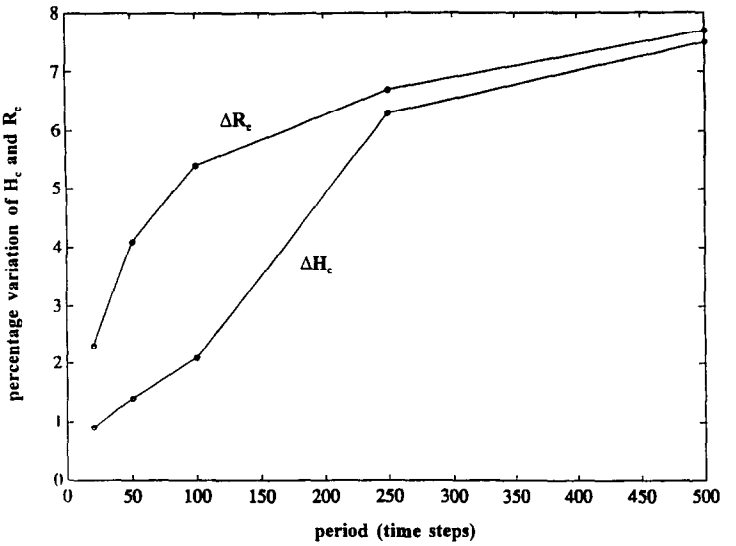

FIG. 7. Characteristics of interface movement with respect to different forcing frequencies of U_p.

quency increases beyond a threshold, the system can no longer respond to it with equal sensitivities. Hence, the predicted trend of the system response is qualitatively verified experimentally [12].

3.3. *Simulation with dynamic contact angle*

Next, we present the results obtained based on a dynamic model for the contact condition at the trijunction point. The model, as schematically depicted in Fig. 3, now allows different values of contact angle according to the instantaneous direction as well as the speed of movement of the trijunction point. Drawing the analogy to the advancing and receding contact angle of a liquid drop on a flat surface [7], two different contact angles are assigned as the asymptotic values for the outward and inward moving cases, respectively. Furthermore, if the contact point moves at a slow enough speed, in the range of $+\varepsilon$ and $-\varepsilon$ as shown in Fig. 3, then the contact angle is allowed to vary between the two asymptotic angles. For the case implemented, we take the asymptotic value of the contact angle associated with the outward moving case to be the same as that adopted in the static model, namely, 135°. The asymptotic contact angle of the inward moving case is taken as 134°, and ε is taken as 0.1. In other words, the variation of contact angle between the inward and outward moving cases is 1°. While this variation seems very small, it has a quite noticeable impact on the characteristics of the solidification process.

Figure 9 shows the comparison of the time histories of both H_c and R_c between the cases with static and dynamic contact conditions, where a perturbation of U_p with a period of $100\Delta\tau$ is enforced. It is striking to observe that with a seemingly small modification of the contact condition, the resulting values of H_c and R_c are substantially affected. For R_c, both time-averaged and fluctuating values are quite different with the two

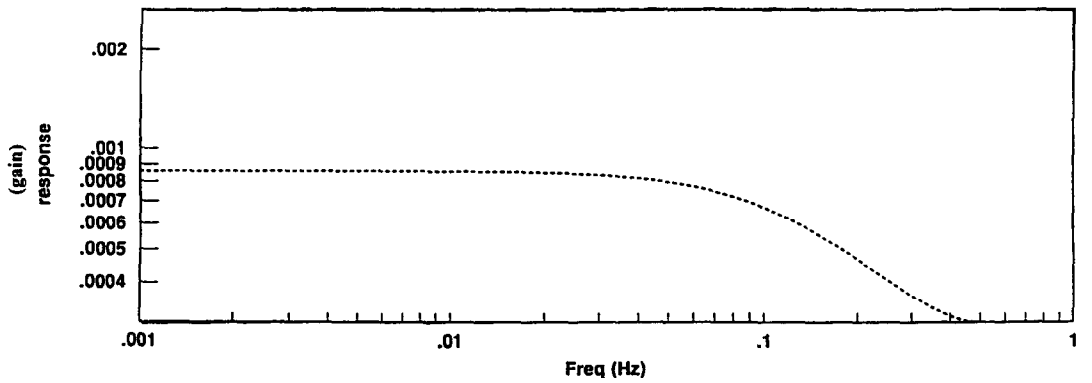

FIG. 8. A typical experimental curve fit of the diameter variation with respect to different forcing frequencies of U_p.

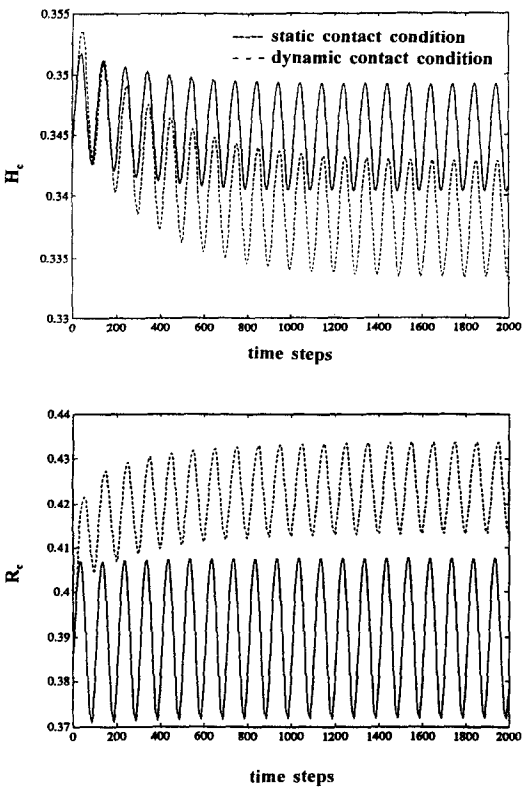

FIG. 9. Time histories of H_c and R_c subject to a single harmonic perturbation of U_p with period = $100\Delta\tau$.

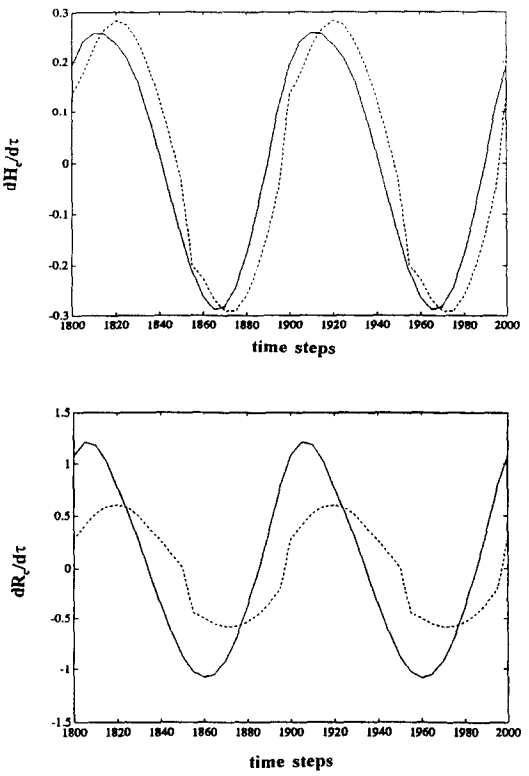

FIG. 10. Time histories of $dH_c/d\tau$ and $dR_c/d\tau$ subject to a single harmonic perturbation of U_p with period = $100\Delta\tau$.

contact conditions; the dynamic contact model yields a crystal of a somewhat larger mean diameter and smaller variations. For H_c, on the other hand, the time-averaged fiber diameter is smaller with the use of the dynamic contact condition; the fluctuating magnitudes in both cases, however, appear quite comparable. Hence, there seem to be differences in behavior between H_c and R_c resulting from the static and dynamic models. In this regard, several points can be noted to elucidate the results observed here. As observed in Fig. 5, the solid/melt interface is concave toward the solid phase, indicating that as the contact angle is reduced, the trijunction point tends to move outward, yielding a larger diameter as shown in Fig. 9. This will also seem to cause a corresponding increase in H_c as seen in the initial transient behavior in the time series plot of H_c. However, a larger crystal diameter also causes a larger volume and a higher heat loss both via conduction and advection. Accordingly, there is also a change in the balance of the thermal constraint at interface, which eventually reduces the value of H_c as observed in the later stage of Fig. 9.

It should be noted that if the solid/melt interface was of the opposite curvature, then the trend of R_c will change as well. Hence, the interaction of thermal and contact condition plays a pivotal role in determining the solidification characteristics. Furthermore, since the contact angle is no longer fixed in the dynamic model, an extra degree of nonlinearity also appears via the enforcement of the contact condition. Plots of the rate of change of H_c and R_c are given in Fig. 10 to demonstrate this point. Clearly, with the static contact condition, a single harmonic reflecting that of the imposed perturbation of U_p is reproduced in both H_c and R_c. On the other hand, with the dynamic contact condition, the movement of trijunction point is no longer consistent with the imposed frequency, instead, it exhibits a quasi-periodic pattern with many additional frequencies present. These additional frequencies appear because contact angles, and hence H_c and R_c, vary in response to the pull speed perturbations.

4. SUMMARY AND CONCLUDING REMARKS

In the present work, a thermocapillary dynamic model has been developed to simulate the EFG process. In developing the present predictive tool, several issues have been identified and addressed, as will be summarized in the following.

It has been established that for the thin fiber growth process, the various control parameters such as the Stefan number, Rayleigh number, Peclet number, and Bond number are far from being order 1. Consequently, care should be exercised in scaling the governing equations to facilitate efficient com-

putations. It is argued that the characteristic velocity scale should be defined to ensure that the solid/melt interface advances at a nondimensional speed of order 1. Since the interface movement is primarily responsible for the nonlinearity of the phase change problem, a conventional choice based on the diffusion scale, choice 1, will yield a set of equations that requires the computing cost to increase by a factor of $1/St$. Similar situations also arise in computations of the solidification characteristics at the morphological scale [9].

Regarding the crystal size variations in response to the pull speed perturbation, a direct linkage between the forcing frequency and the response frequency is observed for both the present case and that of $St = 1$, studied previously [6]. Furthermore, it has also been predicted that as the forcing frequency increases, the solid/melt interface responds at a reduced sensitivity. This trend has been observed experimentally.

Two different models have been utilized for the contact condition at trijunction point, including a conventionally adopted static contact angle [11], and a dynamic model which allows the contact angle to vary according to the direction and the rate of the trijunction point movement. It turns out that the two models can yield substantial differences in the crystal diameter, including the time-averaged as well as the fluctuating magnitudes. Furthermore, additional harmonics can also be yielded by the dynamic contact condition due to the extra nonlinearity contained by it. These observations have clearly indicated that the static contact condition is not sufficient to yield all the information regarding the dynamic behavior of the crystal correctly.

Acknowledgements—The present work is partially supported by the NFS Grant DDM-9213568, and by GE Aircraft Engines. Discussions held with Drs D. G. Backman and Y. Pang have been critical for the successful completion of the present work.

REFERENCES

1. J. P. Kalejs, H. M. Ettouney and R. A. Brown, Comparison of growth characteristics of sapphire and silicon ribbon produced by EFG, *J. Crystal Growth* **65,** 316–332 (1983).
2. J. P. Kalejs, L.-Y. Chin and F. M. Carlson, Interface shape studies for silicon ribbon growth by the EFG technique, *J. Crystal Growth* **61,** 473–484 (1983).
3. G. I. Babbin, E. A. Brener and V. A. Tatarchenko, Crystallization stability during capillary shaping, *J. Crystal Growth* **50,** 45–50 (1980).
4. J. C. Swartz, T. Surek and B. Chalmers, The EFG process applied to the growth of silicon ribbons, *J. Electronic Materials* **4,** 255–279 (1975).
5. E. M. Sachs, Thermal sensitivity and stability of EFG silicon ribbon growth, *J. Crystal Growth* **50,** 102–113 (1980).
6. S.-J. Liang and W. Shyy, Dynamic simulation of thin fiber growth, *J. Materials Processing Manufacturing Sci.* **2,** 189–215 (1993).
7. E. B. Dussan, On the spreading of liquid on solid surface: static and dynamic contact lines, *Ann. Rev. Fluid Mech.* **11,** 371–400 (1979).
8. H. M. Ettouney and R. A. Brown, Finite-element methods for steady solidification problems, *J. Comput. Phys.* **49,** 118–150 (1983).
9. W. Shyy, H. S. Udaykumar and S.-J. Liang, An interface tracking method applied to morphological evolution during phase change, *Int. J. Heat Mass Transfer* **36,** 1833–1844 (1993).
10. W. Shyy, H. S. Udaykumar and S.-J. Liang, A study of meniscus formation with application to edge-defined fiber growth process, *Physics of Fluids A* **5,** 2610–2623 (1993).
11. E. S. Russell, L. C. Filler and D. G. Backman, Intelligent processing of MMC materials, Final Report to DARPA/NRL, Contract No. N00014-90-C-0060, GE Aircraft Engines, Lynn, MA (1992).
12. W. Shyy, *Computational Modeling for Fluid Flow and Interfacial Transport*. Elsevier, Amsterdam, The Netherlands (1994).